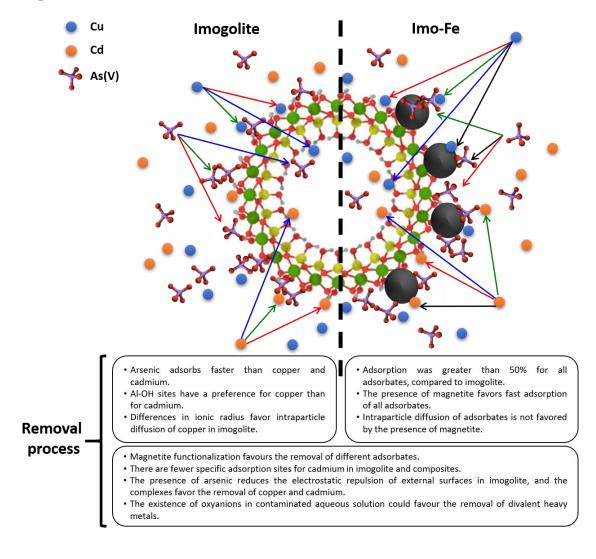1 **Mechanistic insights into simultaneous removal of copper, cadmium and arsenic from**

2 **water by iron oxide-functionalized magnetic imogolite nanocomposites**

3

4 Nicolás Arancibia-Miranda[a,b*], Karen Manquián-Cerda[b], Carmen Pizarro[b], Tamara

5 Maldonado[b], Jonathan Suazo-Hernández[c], Mauricio Escudey[a,b], Nanthi Bolan[d], Binoy

6 Sarkar[e*]

7

8 [a] Center for the Development of Nanoscience and Nanotechnology, CEDENNA, 9170124,

9 Santiago, Chile

10 [b] Facultad de Química y Biología, Universidad de Santiago de Chile, Av. B. O'Higgins, 3363,

11 Santiago, Chile

12 [c] Programa de Doctorado en Ciencias de Recursos Naturales Universidad de La Frontera,

13 (BIOREN-UFRO), Universidad de La Frontera, Avenida Francisco Salazar 01145, Temuco,

14 Chile

15 [d] Global Centre for Environmental Remediation (GCER), Advanced Technology Centre,

16 Faculty of Science, The University of Newcastle, Callaghan, NSW 2308, Australia

17 [e] Lancaster Environment Centre, Lancaster University, Lancaster, LA1 4YQ, UK

18

19 [*]Corresponding author:

20 Dr Binoy Sarkar; Lancaster University; e-mail: b.sarkar@lancaster.ac.uk, and

21 Co-corresponding author:

22 Dr Nicolás Arancibia-Miranda; Universidad de Santiago de Chile; e-mail:

23 nicolas.arancibia@usach.cl

24

25 **Graphical abstract**

Cu
Cd
As(V)

Imogolite   **Imo-Fe**

Removal process

- Arsenic adsorbs faster than copper and cadmium.
- Al-OH sites have a preference for copper than for cadmium.
- Differences in ionic radius favor intraparticle diffusion of copper in imogolite.

- Adsorption was greater than 50% for all adsorbates, compared to imogolite.
- The presence of magnetite favors fast adsorption of all adsorbates.
- Intraparticle diffusion of adsorbates is not favored by the presence of magnetite.

- Magnetite functionalization favours the removal of different adsorbates.
- There are fewer specific adsorption sites for cadmium in imogolite and composites.
- The presence of arsenic reduces the electrostatic repulsion of external surfaces in imogolite, and the complexes favor the removal of copper and cadmium.
- The existence of oxyanions in contaminated aqueous solution could favour the removal of divalent heavy metals.

26

27

2

28 **Highlights**

29 • Imo-Fe$_{50}$ & Imo-Fe$_{25}$ composites showed high efficiency for Cu-Cd-As removal.

30 • Size of magnetite was lower in Imo-Fe$_{25}$ than Imo-Fe$_{50}$.

31 • Magnetic behavior of nanocomposites was confirmed.

32 • Arsenate was removed faster than Cu & Cd by both nanocomposites.

33 • Arsenate favoured the removal of Cu & Cd by both nanocomposites.

34

Abstract

Imogolite and magnetic imogolite-Fe oxide nanocomposites (Imo-Fe$_{50}$ and Imo-Fe$_{25}$, at 50

and 25% Fe loading (w/w), respectively) were synthesized and tested for the removal of

aqueous copper (Cu), cadmium (Cd), and arsenic (As) pollutants. The materials were

characterized by transmission electron microscopy, and specific surface area and isoelectric

point measurements. The Fe-containing samples were additionally characterized by

Mössbauer spectroscopy and vibrating-sample magnetometry. Significant differences were

found in the morphological, electrophoretic, and magnetic characteristics between imogolite

and the nanocomposites. The *in-situ* Fe-oxide precipitation process modified the active

surface sites of the imogolite. The Fe–oxide, mainly magnetite, favored the contaminants'

adsorption over the pristine imogolite. The adsorption kinetics of these pollutants were

adequately described by the pseudo-second order and intraparticle diffusion models. The

kinetic models showed that surface adsorption was more important than intraparticle

diffusion in the removal of the pollutants by all the adsorbents. The Langmuir-Freundlich

model described the experimental adsorption data, and both nanocomposites showed greater

adsorption capacity than the imogolite. The adsorption of Cu and Cd was sensitive to cationic

competition, showing a decrease of the adsorption capacity when the two cations coexisted,

while their adsorption increased in the presence of arsenate.

Keywords: Adsorption; Imogolite; Nanocomposite; Trace Elements; Water Treatment.

1. Introduction

The impact and harmful effects to human health generated by the presence of pollutants in the environment is a highly relevant issue within the context of treatment and management of water resources. The increasing difficulty to satisfy basic water requirements, and the anthropogenic origin of numerous pollutants, make it necessary to ensure the supply of quality water to the world's growing population [1–3]. It is estimated that more than 150 million people in the world are exposed to high concentrations of potentially toxic trace elements (TEs) like cadmium (Cd), copper (Cu), and arsenic (As) [4–10], because these pollutants are present in both the ground- and surface water sources. Industrial wastewater discharge, mining and agricultural activities are important anthropogenic sources which contribute to increasing amount of TEs in the environment [11–13]. In addition to the direct addition from industrial wastewater, mining activities add TEs to the environment through the residues generated by ore extractions (low grade ores) and purification (tailings) processes, whereas agricultural activities add through the constant application of fertilizers, biosolids, and soil amendments, severely modifying the biogeochemical cycles of the elements within the ecosystem [10,14–18]. Untreated effluents from industrial wastewater, mining and agricultural activities contain high concentrations of TEs, which have a direct negative effect mainly on the aquatic life [11–13]. Copper (Cu), Cd, and As stand out among this group of pollutants because of their widespread occurrence in polluted waters and high degrees of toxicities [2,10,11,13-15]. Their effects on human health are various, for example, Cu and Cd are responsible for pathological symptoms such as cirrhosis, generalized hemolysis, hepatic necrosis, generalized weakness, pulmonary edema, fertility problems, and different types of cancer [19,20]. Cd is specifically responsible for bone damage, commonly associated with the Itai-Itai disease, described for the first time in Japan in 1940 [20,21]. Arsenic (As) causes even more damage than Cu and Cd due to its genotoxic and cytotoxic

81 characters and ability to induce epidemiological toxicity, causing arsenicosis, diabetes

82 mellitus, peripheral vascular diseases, and various types of cancer, among other disorders [2].

83 The World Health Organization (WHO) indicates that the concentrations of these elements in

84 water for human consumption should not exceed 1.5 mg·L^{-1} for Cu, and 0.01 mg·L^{-1} for Cd

85 and As [22].

86 Considering the extensive problem caused by the presence of TEs in aqueous matrices, a

87 considerable number of investigations have focused on the search, design, and application of

88 different types of removal techniques (e.g., adsorption, absorption, precipitation, and co-

89 precipitation), using physical and/or chemical processes [23]. In this context, the use of

90 different nanostructured substrates, such as Fe nanoparticles (e.g., nano-scale zero valent iron

91 (nZVI)), TiO_2, graphene, clay minerals, among others, has been a subject of intense research

92 [24–26].

93 Imogolite, a nanotubular aluminosilicate, is found in the inorganic phase of soils of volcanic

94 origin, and it has shown a high ability for the removal of pollutants due to its wide versatility,

95 high adsorption capacity, and easy functionalization [27–32]. Imogolite's stoichiometry is

96 $(OH)_3Al_2O_3SiOH$, with 100 nm length, and average outer and inner diameters of 2.0 and 0.9

97 nm, respectively [33,34]. This aluminosilicate has a marked superficial differentiation, where

98 aluminol groups ($\equiv$Al-OH ($pK_{a1}=9.9$ and $pK_{a2}=11.9$)) predominate on the outer surface, while

99 silanol groups ($\equiv$Si-OH ($pK_{a1}=-2.77$ and $pK_{a2}=6.77$)) constitute the inner surface [18,35]. The

100 differential pKa values owing to the unique aluminol and silanol structures, as mentioned

101 above, allow imogolite having positive charges on its outer surface over wide pH values,

102 while on the inner surface the predominant charge is negative. The behavior of the surface

103 groups of imogolite would facilitate the simultaneous removal of anions and cations,

104 respectively, a phenomenon recently described in the literature [18,35,36]. Despite of the

105 surface properties and flexibility of synthesis, imogolite was scarcely used in

106 decontamination studies, with the adsorption of Ni^{2+}, and degradation of azo compounds by

107 means of Photo-Fenton reactions standing out, using Ge-imogolite and Fe-imogolite,

108 respectively, whose nanostructures were isomorphic with that of imogolite [31,37]. A recent

109 study by Arancibia-Miranda et al., showed that the functionality of imogolite with Fe-oxides

110 favored the removal kinetics of arsenate, besides facilitating an energy-neutral separation of

111 the adsorbent due to magnetic characteristics [28]. Currently there is no information on the

112 variation of the ability to remove pollutants in multi-component systems by imogolite where

113 the chemical properties of pollutants can give rise to synergistic or antagonistic effects in the

114 contaminant removal performance [38].

115 This work, therefore, studied the removal of Cu, Cd, and As (arsenate) from contaminated

116 water by magnetite-imogolite nanocomposites (Imo-Fe), a recently developed material. The

117 specific objectives are: (i) to evaluate the simultaneous removal of Cu, Cd, and As by Imo-Fe

118 nanocomposites, and (ii) to study the possible removal mechanisms and interactions of Cu,

119 Cd, and As present in aqueous systems with the nanocomposites.

120

121 **2. Materials and methods**

122 2.1 Reagents

123 The imogolite sample used in this study was prepared using tetraethyl orthosilicate,

124 (99.995%, Sigma–Aldrich), NaOH (99.996%, Merck), and $Al(NO_3)_3 \cdot 9H_2O$ (99.998%,

125 Merck). The oxidic coatings of Fe was synthesised using KNO_3 (99.998%, Merck),

126 $FeSO_4 \cdot 7H_2O$ (99.998%, Merck) and NH_4OH (99.997%, Sigma–Aldrich). In adsorption

127 studies, solutions of $Cd(NO_3)_2$, $Cu(NO_3)_2$ and As (As_2O_5 in H_2O) were prepared from

128 commercial standards (Titrisol®).

129

2.2 Synthesis of imogolite

Tetraethyl orthosilicate (TEOS) was added to a 5 mM aqueous solution of $Al(NO_3)_3·9H_2O$ until an Al:Si ratio of 2:1 was reached. Then a 0.1 M NaOH solution was added at a rate of 1.0 mL min^{-1} until an Al:Si:OH ratio of 2:1:4 was obtained. The mixture was stirred for 60 min, and then heated at 95 °C for 5 days. Once the aging process was completed, the resultant mixture was cooled down to ambient temperature. A 0.1 M NH_4OH solution was added rapidly until a pH of about 8.0 was reached. The solid was concentrated by centrifugation of the suspension at 9000 rpm for 30 min, and it was washed with double distilled water until the washings reached an electric conductivity of less than 0.78 dS·m^{-1} [39,40].

2.3 Synthesis of iron oxide and preparation of imogolite-iron nanocomposite

To obtain a magnetic Fe-oxide, 0.250 g of $FeSO_4·7H_2O$ was dissolved in 20.0 mL of double-distilled water which was made O_2-free by flowing with N_2. Then 0.033 g of KNO_3, and 0.5 mL of concentrated NH_4OH were added to precipitate the Fe-oxide from the above solution. The magnetic nanocomposites (hereafter Imo-Fe$_{50}$ and Imo-Fe$_{25}$, at 50 and 25% Fe loading (w/w), respectively) were prepared according to a procedure described by Arancibia-Miranda et al. [21].

2.4 Characterization

The products were characterized by transmission electron microscopy (TEM), and isoelectric point (IEP), electrophoretic mobility (EM), and Brunauer–Emmett–Teller (BET) specific surface area (SSA) measurements. Fe-containing samples were additionally characterized by Mössbauer spectroscopy, and vibrating-sample magnetometry (VSM) and SQUID magnetometer.

The samples were observed with a Zeiss EM 910 transmission electron microscope (Zeis,

Germany) using 80 kV-acceleration potential. Sample suspension was deposited on a thin

layer of carbon, and the solvent was dried via vacuum evaporation. The carbon film was then

transferred to a perforated Cu support grid for collecting the images.

The SSA of imogolite and both nanocomposites was measured by the N_2 method of

Brunauer-Emmett-Teller (BET), and pore size was calculated from the Barrett, Joyner and

Halenda (BJH) analysis of N_2 adsorption/desorption isotherms at 77 K using an automatic

analyser (Quantachrome Nova Station A, Quantachrome, USA, Florida).

The ^{57}Fe Mössbauer analysis was conducted at 298 K with a transmission acceleration

constant setup with a ~30 mCi ^{57}Co/Rh source, and α-Fe as reference. Data were collected

using a System MS4 spectrometer (Ligth Machenary, USA). Data were stored in a 512-

channel MCS memory unit, with a Doppler velocity ranging around ± 10 mm.s^{-1}. The

experimental data were fitted to Lorentzian functions (least-square method) using the

NORMOS^{TM} program algorithm.

The IEP was determined by measuring the EM (at pH = 5 to 11) under constant stirring of

suspensions on a Zeta Meter 4.0 apparatus (Zeta-Meter, USA, Stauton). About 100 mg of

each sample was suspended in 200 mL of a solution with an ionic strength of 1.0×10^{-3} M

(KNO$_3$). The IEP was obtained from the EM vs. pH graph as the pH at which EM = 0. The

Helmholtz-Smoluchowski equation was applied for the conversion of EM to zeta potential

(ZP), when this parameter was required [41].

The magnetic response was investigated with a vibrating sample magnetometer (VSM)

(homemade) operated at room temperature with a maximum magnetic field of 1.2 Tesla, and

a sensitivity of 10^{-4} emu.

2.5 Batch adsorption experiments

180 The adsorption kinetics were carried out at 25±2 °C. Working solutions of the TEs were

181 prepared by dilution in Milli-Q water of stock solutions of 1000 mg·L^{-1} of Cd^{2+}, Cu^{2+} and As

182 (arsenate), from commercial standards (Titrisol$^{®}$). In the kinetic studies, 50 mg of samples

183 were added to 20 mL of the TE solutions (Cd and Cu: 50 mg·L^{-1}, and arsenate: 350 mg·L^{-1};

184 pH=5.0±0.2) using 1.0x10^{-3} M KNO$_3$ as the background electrolyte. The concentration of

185 TEs in the suspension was determined at 5, 10, 20, 30, 45, 60, 90, 120, 150, and 180 min

186 intervals after separation of the solids as described later.

187 In the one-component adsorption isotherm studies, 50 mg of the samples were added to 20

188 mL of solution containing Cd or Cu (0–100 mg·L^{-1}) or arsenate (0–200 mg·L^{-1}), at pH

189 =5.0±0.2) using 1.0x10^{-3} M KNO$_3$ as the background electrolyte with a stirring time of 180

190 min. The concentration ranges of contaminant elements were chosen to simulate real mining

191 wastewater concentrations of these elements often encountered in Chile [14,18]. The effect of

192 competition of different TEs alone was assessed only in the studies of adsorption isotherms,

193 using a mixture containing, for each TE, the same concentration considered in one-

194 component systems [11]. The adsorption experiments were carried out at 25±2 °C. The

195 adsorption of the adsorbates in multi-component systems considered the presence of Cu and

196 Cd at similar concentrations (0-100 mg·L^{-1}, treatment 1), and the adsorption of those metals

197 at the same previous concentrations was also evaluated, but in the presence of arsenate (0-100

198 mg·L^{-1}, treatment 2). The pH of each suspension was adjusted to 5.0±0.2 by the addition of

199 HNO$_3$ or KOH (1.0x10^{-1} mol·L^{-1}).

200 The samples were centrifuged at 10,000 rpm for 30 min followed by filtration of the

201 supernatant through 0.22 μm Millex-GX membranes. Elements in the clear supernatant were

202 then analysed by Inductively Coupled Plasma-Optical Emission Spectroscopy (ICP-OES,

203 Perkin Elmer Optima 2000). Eq. 1 gave the amounts of adsorbed ions, as the difference

204 between their initial and final concentrations in solutions.

205 $$q_t = \frac{(C_0 - C_t) \cdot V}{M} \text{ (Eq. 1)}$$

206 where, C_0 and C_t are respectively the initial and equilibrium concentrations of TEs ($mg \cdot L^{-1}$)

207 at time "t", V (L) is the volume, M (g) is the mass of the adsorbent, and C_t is the amount

208 adsorbed ($mg \cdot g^{-1}$). All the adsorption tests were carried out in triplicate, and average values

209 were reported.

210

211 2.6 Theory

212 The pseudo-first order model (PFO), pseudo-second order model (PSO), and intraparticle

213 diffusion model, were used to analyse the adsorption kinetics of Cd, Cu, and arsenate on

214 imogolite, Imo-Fe$_{25}$ and Imo-Fe$_{50}$ [10,18,42,43].

215 The PFO rate equation is given as Eq. 2 [10,18,42,43]:

216 $$\frac{dq}{dt} = k_1 \cdot (q_e - q_t) \text{ (Eq. 2)}$$

217 where, q_e and q_t correspond to the amounts of solute adsorbed at the equilibrium and at time t

218 (expressed in ($mg \cdot g^{-1}$)), respectively. k_1 (min^{-1}) is a combination of adsorption (k_a) and

219 desorption (k_d) constants [10,18,42,43].

220 The expression of the PSO kinetic model can be written as Eq. 3 [10,18,42,44,45]:

221 $$\frac{dq}{dt} = k_2 \cdot (q_e - q_t)^2 \text{ (Eq. 3)}$$

222 where, k_2 is the PSO adsorption rate constant ($g \cdot mg^{-1} \cdot min^{-1}$). From this model, the parameter

223 h ($mg \cdot g^{-1} \cdot min^{-1}$), which accounts for the initial adsorption rate, and is defined as $h = k_2 \cdot q_e^2$,

224 can be calculated.

225 The Webber-Morris model, also known as the intraparticle diffusion model or pore-diffusion

226 model, is a single-resistance model derived from the Fick's second law of diffusion [46]. The

227 mathematical expression that defines this model is (Eq. 4):

228 $$C_t = k_{int} t^{1/2} + C \qquad (Eq. 4)$$

229 where, k_{int} (mg·g^{-1}·min$^{-1/2}$) is the intraparticle diffusion constant, and C (mg·g^{-1}) is a constant

230 related to the thickness of the surface layer [18,47]. The higher the value of C, the greater the

231 boundary layer effect, which is related to intraparticle diffusivity.

232

233 2.7. Residual error analysis

234 To evaluate the fit of kinetic and isotherm equations to the experimental data [18,24], the

235 residual root mean square error (RMSE) can be defined as (Eq. 5):

236 $RMSE = \sqrt{\frac{1}{N-2}\sum_{i=1}^{N}(q_{e(exp)} - q_{e(cal)})^2}$ (Eq. 5)

237 The subscripts "exp" and "calc" show the experimental and calculated values, and N is the

238 number of observations in the experimental data; the smaller the RMSE value, the better the

239 curve fitting.

240

241 **3. Results and Discussion**

242 3.1 Sample characterization

243 The presence of magnetite in the nanocomposites was confirmed by Mössbauer spectroscopy

244 (Supplementary Material; Fig. S1). Differences were found in the percentages of Fe-oxide in

245 both the nanocomposites, where Imo-Fe$_{25}$ showed a slight increase in the hyperfine

246 parameters of magnetite compared to Imo-Fe$_{50}$ (Table S1), mainly in the relative sub-spectral

247 area (RA). The relative isomeric change of αFe suggested that greater coverage proportions

248 would favor the oxidation of the Fe-oxide. In the spectra of both nanocomposites, the

249 presence of a marked doublet was seen, which was attributed to the presence of

250 superparamagnetic Fe^{3+}, indicating that a fraction of the Fe used in the coverage was not part

251 of the magnetite (Fig. S1), and this was more evident in Imo-Fe$_{50}$ than Imo-Fe$_{25}$ [20].

252 The nanocomposites obtained were characterized morphologically using TEM (Fig. S2),

253 estimating their dimensions from measures of multiple particles as 70 to 90 nm, with a mean

254 value of 82±3 nm. In the case of imogolite, dispersed nanotubular structures were seen, due

255 to the fact that the nanotubes were highly dispersed at the pH (pH=4.00±0.20) at which the

256 measurements were made [48]. The average outer diameter of imogolite was 2.11±0.02 nm,

257 while its length was greater than 500 nm, in agreement with previous observations

258 [18,28,49], with a low by-product content. No morphological changes were seen in imogolite

259 due to the effect of Fe-oxide coverage, but the synthesis conditions of the Fe-oxide caused a

260 high agglomeration in the nanotubes (Fig. S2). The Fe-oxide supported on the Imo-Fe$_{25}$

261 nanocomposite showed a diameter distribution between 16 and 46 nm, with a mean value of

262 36±4 nm. In the case of Imo-Fe$_{50}$, the dimensions of the Fe-oxide nanoparticles were found

263 between 20 and 50 nm, with a mean value of 44±3 nm [21]. The distribution of Fe-oxide

264 immobilized on the surface of the imogolite was sensitive to the degree of coverage, finding

265 greater homogeneity of the oxides in the Imo-Fe$_{25}$ nanocomposite compared to Imo-Fe$_{50}$.

266 This phenomenon was similar to what was described in clay minerals covered with nZVI

267 particles [24,50], associated with limited Fe^{3+} adsorption sites that imogolite possessed. IEP

268 values calculated from the EM measurements [21] were 10.1, 6.4, 8.9, and 7.7, respectively,

269 for imogolite, magnetite, Imo-Fe$_{25}$, and Imo-Fe$_{50}$ (Fig. 1). According to Eq. 6, the apparent

270 surface coverage (ASC) of Fe-oxide on the imogolite surface was worked out by considering

271 the zero point charge (ZPC; of magnetite), the molecular weights of imogolite (M_s=198.08

272 g·mol^{-1}) and iron oxide (M_M=231.54 g·mol^{-1}), as well as the IEP of both the nanocomposites

273 [21].

274 $$ASC = \frac{(IEP_S - ZPC) \cdot M_S^{-1}}{[(M_M^{-1} - M_S^{-1}) \cdot (ZPC - IEP_S) + M_M^{-1} \cdot (IEP_S - IEP_M)]} \cdot 100 \quad \text{(Eq. 6)}$$

275 The Fe-oxide coating was close to 20 (Imo-Fe$_{25}$) and 32 mass% (Imo-Fe$_{50}$), lower than

276 stoichiometrically planned (25 and 50 mass%). However, the ASC for Imo-Fe$_{25}$ was closer to

277 the theoretical value, indicating that the coverage process was more homogeneous when a

278 lower Fe percentage was used. This was due to the finite number of sites where Fe could be

279   adsorbed on imogolite, a result consistent with what was seen in the microscopic analysis

280   (Fig. S2). These results suggested that higher concentrations of Fe might form multilayers,

281   affecting the proportional variations of IEP and ASC [28,51].

282   The microporous structure of imogolite, Imo-Fe$_{25}$, and Imo-Fe$_{50}$ was studied by N$_2$

283   adsorption-desorption, and it was found that the SSA of imogolite (350 m$^2\cdot$g^{-1}) [52,53]

284   decreased significantly in both the nanocomposites, and was 15% lower for Imo-Fe$_{25}$, and

285   35% lower for Imo-Fe$_{50}$, compared to the pristine imogolite (Table S2) [54].

286   Differences in the size and distribution of magnetite as a consequence of Fe concentrations

287   applied in the coverage process caused changes in the magnetic behaviour of the

288   nanocomposites too (Fig. S3). A saturation of magnetization was obtained after an applied

289   magnetic field of 8000 kOe, and it was 92.14 emu$\cdot$g^{-1} for magnetite, but decreased drastically

290   in the nanocomposites, with values of 6.82 emu$\cdot$g^{-1} for Imo-Fe$_{25}$, and 11.23 emu$\cdot$g^{-1} for Imo-

291   Fe$_{50}$ [24,28,55]. The coercive fields (Hc) were 53.05 Oe for Imo-Fe$_{25}$, and 57.89 Oe for Imo-

292   Fe$_{50}$, while this parameter for pure magnetite was 142.81 Oe. The remanence data indicated

293   that this parameter was significantly greater in magnetite (~11 emu$\cdot$g^{-1}) with respect to the

294   nanocomposites, and it was about 25 times greater compared to that obtained for Imo-Fe$_{25}$

295   (0.33 emu$\cdot$g^{-1}) and Imo-Fe$_{50}$ (0.56 emu$\cdot$g^{-1}). Despite the evident differences in the magnetic

296   parameters between magnetite and both the nanocomposites, the values obtained, mainly the

297   saturation magnetization, allowed classifying them as clearly magnetic materials (Fig. S3).

298   Evolution of the coercive field as a function of temperature for Imo-Fe$_{25}$ and Imo-

299   Fe$_{50}$ showed increased values at decreased temperatures. For Imo-Fe$_{25}$, the increase in

300   coercivity was evident at temperature close to 75 K, while for Imo-Fe$_{50}$ this parameter

301   increased to approximately at 100 K. These results supported that the magnetite nanoparticles

302   constituting the nanocomposites were smaller in Imo-Fe$_{25}$ than Imo-Fe$_{50}$, because at

303   temperatures exceeding 100 K the magnetization of Imo-Fe$_{25}$ was more unstable than Imo-

304   Fe$_{50}$ (Fig. S3).

305

306   3.2 Kinetic adsorption

307   *3.2.1 Cadmium and copper*

308   The equilibrium time was 60 min of reaction for the adsorption of Cu and Cd on magnetite,

309   imogolite and both nanocomposites (Fig. 2). The PSO model adequately described the

310   adsorption kinetics of the TEs. The PSO model gave correlation coefficients ($r^2 \geq 0.990$)

311   greater than those estimated by the PFO models, and the values of q_e were close to the

312   experimental ones (Table 1).

313   The values of the initial adsorption constant (h), when q_t/t approaches zero, showed a

314   difference between the nanocomposites. This parameter increased considerably for Imo-Fe$_{25}$

315   and Imo-Fe$_{50}$ compared to magnetite and imogolite, due to the formation of new adsorption

316   sites ($\equiv$Fe-OH) on the nanocomposites [24,28]. The newly developed adsorption sites favored

317   the rapid adsorption of TEs by the nanocomposites, as it was observed for the case of Cu and

318   Cd (Fig. 2).

319   The diffusion of Cu and Cd on both nanocomposites was compared by the intraparticle

320   diffusion model proposed by Weber and Morris [18,24,47], finding differences in the values

321   of the parameters given by this model (Table 1). The differences possibly were as a

322   consequence of the imogolite-Fe oxide surface coverage process (Fig. 3). The multiple curves

323   seen in Fig. 3 indicated that the adsorption took place by three probable steps [56]. The first

324   one was a surface adsorption or film diffusion (step I). Adsorption through an intraparticle

325   diffusion mechanism was evidenced by the second linear zone of the graph (step II), while

326   the last step corresponded to adsorption on the inner sites of the adsorbent (step III). By

327   means of this model, it could be inferred that the adsorption of Cu and Cd on imogolite and

328   both nanocomposites took place at the first stage through surface diffusion, where the largest

329   proportion of these elements was adsorbed, with the highest adsorption values obtained with

330   Imo-Fe$_{25}$ and Imo-Fe$_{50}$ [18,24,47].

331

332   *3.2.2 Arsenate*

333   The kinetic adsorption behavior of arsenate in case of all the studied materials was described

334   adequately by the PSO model (Fig. 3), where parameter h was slightly sensitive to the

335   coverage process, indicating that the presence of Fe-oxide favored the adsorption in short

336   adsorption times (Table 1). The intraparticle diffusion model for arsenate in case of the

337   studied adsorbents showed that surface adsorption was the predominant process [18,24,47].

338   This behavior could be explained by the strong specific interaction of the surface groups of

339   imogolite and magnetite ($\equiv$Al$_2$-OH, $\equiv$Al-OH, and $\equiv$Fe-OH) with arsenate, possibly involving

340   a ligand exchange mechanism, as described in the literature [57].

341   In general, the surface coverage process of imogolite with Fe-oxide gave rise to a synergic

342   effect on the removal of the adsorbates. There could even be a blockage of the inner surface

343   of imogolite by Fe^{3+} used during the synthesis of magnetite, which mainly affected the

344   removal of Cu and Cd. The blockage of inner surfaces by Fe^{3+} contributed to the variation of

345   surface charges of the nanocomposites, and the high affinity of Fe-oxides for arsenate (log K

346   ((FeO)$_2$AsO$_4$$^{3+}$)=27.1) compared to the affinity that arsenate had with Al (log K

347   (AlO$_4$AsH$_2$)=9.72) [58,59].

348

349   3.3 Adsorption isotherms

350   The removal of Cu, Cd and arsenate by imogolite, magnetite, Imo-Fe$_{25}$, and Imo-Fe$_{50}$ was

351   analysed by the Langmuir-Freundlich (Eq. 7) isotherm model [10,60].

352    $$q = \frac{Q_{sat}(K \cdot C_e)^m}{(K \cdot C_e)^m + 1} \text{ (Eq. 7)}$$

16

353 The Langmuir-Freundlich parameters were obtained by nonlinear least-square regression

354 analysis, in which Q_{sat} is the adsorption capacity of the system (mg of adsorbate·g^{-1}

355 adsorbent), K correspond to the affinity constant for adsorption (L·mg^{-1}), C_e (mg·L) is the

356 equilibrium adsorbate concentration, and *m* is the index of heterogeneity.

357 The experimental data showed a high level of fitting to the Langmuir-Freundlich model, with

358 $r^2 \geq 0.990$, indicating that they adequately represented the adsorption behavior of the studied

359 TE species (Tables 2 and 3).

360

361 *3.3.1 Adsorption of copper and cadmium*

362 In general, the adsorption of Cu and Cd on both the nanocomposites was higher than on

363 imogolite and magnetite, for all the treatments. The maximum adsorption of Cu and Cd on

364 Imo-Fe_{50} (Table 2) suggested that an increased ASC of Fe-oxide favored the adsorption of

365 both adsorbates, most likely due to the decrease of the electrostatic repulsion, and because of

366 the presence of new functional groups ($\equiv$Fe-OH). These behaviors could be confirmed by the

367 reduction of EM values at working pH ranges with increasing Fe-oxide coverages, from

368 EM=2.78 (+33.30 mV) for imogolite to EM=2.32 (+27.79 mV) for Imo-Fe_{25}, and EM=1.58

369 (+18.93 mV) for Imo-Fe_{50} [41]. The relative reduction of surface positive charge resulted in a

370 reduction of electrostatic repulsion, consequently increasing the adsorption of Cu and Cd

371 (Fig. 4) [21]. Furthermore, all the materials showed a high capacity for removing Cu than Cd.

372 This was reflected by the values of C_m, which were 50% greater for Cu than those determined

373 for Cd (Table 2). However, the adsorption intensity of Cd, as reflected by the values of K,

374 was greater than Cu for all the studied substrates (Table 2), showing that Cd was adsorbed on

375 the high energy sites. The shapes of the adsorption curves in one-component systems were

376 different for each metal; in the case of Cu, they were of the *L* type, while for Cd they were of

377 the *S* type, reflecting different interactions that occurred between the surface sites of

378 imogolite or nanocomposites and the adsorbates [37,60–62].

379 In the case of multi-component systems, the behavior was similar to that of the one-

380 component systems, both with respect to the type of adsorption curves (type *L* for Cu, and

381 type *S* for Cd) and adsorption capacities. Higher adsorption capacities of the nanocomposites

382 for both metals were observed compared to the imogolite, with Cu again showing a greater

383 adsorption than Cd (Table 2). However, the most noticeable effect of the competition was the

384 increased value of the *K* constant, which was particularly sensitive for Cu (Table 2),

385 especially in the case of imogolite, whose value was seven times greater in the competitive

386 system than that in the one-component system [15]. For Cd, the constant *K* showed an

387 increase in the case of imogolite, with a value 50% greater in the competitive system than

388 that in the one-component system. In case of the nanocomposites, no important variations

389 were seen. The behavior found for imogolite indicated that the adsorption of both the metals

390 in a competitive system occurred on sites of greater specificity, with a preference for Cu, a

391 phenomenon similar to that reported by Clark and McBride [62].

392 The presence of arsenate in the solution substantially changed the removal of both the metals

393 (Fig. 4c and f), showing an increase of the adsorption capacity for Cu and Cd on the studied

394 materials. The increase was predominant in case of the nanocomposites where the presence of

395 magnetite influenced this phenomenon (Table 2). This behavior could be explained by the

396 fact that arsenate was adsorbed more readily than both metals, as determined in the kinetic

397 studies, generating a kind of functionalization of the adsorbent's surface that changed the

398 system's surface charge, making it less negative. This likely allowed to overcome the

399 electrostatic barrier generated between arsenate and the surface of the adsorbents [10,63,64].

400 The types of curves of both metals in the presence of arsenate did not show large variations

401 compared to the Cu/Cd multi-component system, but the affinity constant K showed an

402 increase of greater than 10% due to the presence of arsenate.

403

404 *3.3.2 Adsorption of arsenate*

405 The adsorption isotherms of arsenate on imogolite, Imo-Fe$_{25}$, and Imo-Fe$_{50}$ are shown in Fig.

406 5. The Langmuir-Freundlich model showed the best fit of the experimental data ($r^2 \geq 0.955$)

407 (Table 3). For the two studied systems, single- and multi-components, the curves of the

408 isotherms were of the S type, showing a good affinity between different substrates and

409 arsenate. The adsorption capacity (Q_{sat}) was greater for the magnetic materials than for

410 pristine imogolite (Table 3), indicating that the adsorption of arsenate was strongly

411 influenced by the type of surface of the substrates. The presence of Cd and Cu affected the

412 adsorption capacity for arsenate of the materials, showing an approximately 20% decrease

413 compared to the one-component system. This behavior could be due to the possible changes

414 in adsorption rates, which would occur when all adsorbates were present in the system,

415 enabling Cd and Cu to occupy surface sites of the adsorbents at times similar to that of

416 arsenate [65,66]. The values of the affinity constants K obtained from the Langmuir-

417 Freundlich model turned out to be highly sensitive to the coverage process as well as to the

418 presence of the bivalent metals, showing an increased magnitude on Imo-Fe$_{25}$ and Imo-Fe$_{50}$

419 compared to imogolite. This effect was slightly greater in the magnetic materials when the

420 three adsorbates coexisted, suggesting that in the competitive system, arsenate (an oxyanion)

421 was adsorbed through a ligand exchange mechanism on the specific surface sites present in

422 imogolite and magnetite. Similar results were reported in case of clay minerals and

423 nanoparticles, where the pH and variation of surface charge favored such adsorption

424 mechanism [10,63,64].

425

426 3.4 Environmental implications and physicochemical properties of magnetite-imogolite

427 nanocomposites

428 This paper provided new information on the characteristics of imogolite as a support for the

429 immobilization of magnetite. The size and distribution of magnetite nanoparticles did not

430 depend exclusively on the presence of the aluminosilicate, rather the concentration of Fe^{3+}

431 was a critical factor to consider, where higher amounts of Fe^{3+} favored a three-dimensional

432 growth of Fe-oxides with the formation of multilayers [21]. Our results indicated that the

433 nanocomposites removed about 100% more TEs than imogolite, where the immobilization of

434 Fe oxide on imogolite was achieved through a simple step, and with minimum technical

435 requirement [67]. These observations placed Imo-Fe$_{25}$ and Imo-Fe$_{50}$ as alternative and cost-

436 effective adsorbents for the elimination of TEs from aqueous systems with variable

437 contaminant contents.

438 The immobilization of Fe oxide on imogolite modified the SSA values in both

439 nanocomposites, as compared to imogolite, resulting in 15 and 34% decrease of SSA in Imo-

440 Fe$_{25}$ and Imo-Fe$_{50}$, respectively. Despite these results, both nanocomposites showed higher

441 Cu and Cd removal capacities, as a consequence of higher availability and affinity of the

442 newly generated surface sites. Further, the composition of the aqueous solution significantly

443 affected the removal of the adsorbates, with changes observed in the rate, capacity and

444 intensity of removal of Cu, Cd, and arsenate (Fig. 5).

445 The data obtained from the adsorption studies, mainly from the isotherms, showed that in

446 imogolite there were at least four kinds of adsorption sites which held variable selectivity for

447 metals [68–70]. These sites could be categorized as follows: preferential sites for Cu,

448 preferential sites for Cd, preferential sites for arsenate, and non-preferential sites for Cu, Cd

449 or arsenate. In this context, our results showed that in multi-component systems (in which Cu

450 and Cd coexisted), imogolite had a marked preference for Cu over Cd. The decrease of the

451 adsorption capacity of Cu in the competitive system was 12% compared to the single

452 component system, while that for Cd exceeded 41% in the same case. These differences

453 might be associated with the chemical characteristics of each metal ion, where the ionic

454 radius, polarizability, and electronegativity (EN) would condition their affinity towards $\equiv$Al-

455 OH and $\equiv$Si-OH groups. This has been seen in similar systems where the most adsorbed

456 metal had the highest EN (Cu_{EN}=1.90 vs. Cd_{EN}=1.62) [71]. In the case of nanocomposites, the

457 behavior was similar to that found for imogolite, but the Fe-oxide coverage process caused a

458 slight decrease in the Cd adsorption difference between the single- and multi-component

459 systems. This was probably caused by electrostatic effects, presence of $\equiv$Fe-OH groups, and

460 changes in the porosity of the nanocomposites [10,15,57].

461 The presence of arsenate in the competitive system altered the general adsorption behavior of

462 Cu and Cd on different substrates, which was evidenced by the increase of the value of

463 constant K (Table 2). The adsorption of arsenate modified the affinity and selectivity of the

464 original active sites of imogolite and nanocomposites, which might have reduced the density

465 of common sites for Cu and Cd, but generated specific sites for each metal. This would also

466 affect the macroscopic behavior of the adsorption, as observed by the changes of values of

467 the adsorption constants and types of isotherm curves [47, 58-60].

468

469 **4. Conclusions**

470 The Fe oxide-functionalized magnetic imogolite nanocomposites showed better TE removal

471 capabilities than the pristine imogolite, and the removal capacity varied according to the

472 amount of magnetite contained in the nanocomposites. Due to an increasing coverage with Fe

473 oxide, there was a decrease of IEP, which was associated with a reduction of the positive

474 surface charge at equilibrium pH for both the nanocomposites, as compared to the pristine

475 imogolite. The reduction of positive surface charge favored the adsorption of cationic

476 adsorbates (Cd^{2+} and Cu^{2+}) due to a smaller electrostatic repulsion between the adsorbent and

477 adsorbates, and through complexing the adsorbates on the surface functional groups.

478 The adsorption studies showed that the composition of the equilibrating solution strongly

479 influenced the adsorption of Cu, Cd, and arsenate on imogolite as well as on its magnetic

480 nanocomposites (Imo-Fe$_{25}$ and Imo-Fe$_{50}$). The presence of arsenate favored the removal of

481 divalent metals such as Cu and Cd. This study showed that Imo-Fe$_{25}$ and Imo-Fe$_{50}$ were

482 efficient nanocomposites for the removal of trace elements such as Cu, Cd, and arsenate,

483 even in systems where there was competition for the adsorption sites. These new adsorbents

484 are thus a group of promising and efficient materials for TE removal from aqueous solutions,

485 which could be used in conventional filter systems.

486

491

492 **References**

493 [1] R.A. Crane, T.B. Scott, Nanoscale zero-valent iron: future prospects for an emerging

494   water treatment technology, J. Hazard. Mater. 211–212 (2012) 112–125.

495 [2] P.Smedley, D. Kinniburgh, A review of the source, behaviour and distribution of

496   arsenic in natural waters, Appl. Geochem. 17 (2002) 517–568.

497 [3] X. Li, D.W. Elliott, W. Zhang, Zero-valent iron nanoparticles for abatement of

498   environmental pollutants: materials and engineering aspects, Crit. Rev. Solid State

499   Mater. Sci. 31 (2006) 111–122.

500 [4] E. Galunin, J. Ferreti, I. Zapelini, I. Vieira, C. Ricardo Teixeira Tarley, T. Abrão, M.J.

Santos, Cadmium mobility in sediments and soils from a coal mining area on Tibagi River watershed: environmental risk assessment, J. Hazard. Mater. 265 (2014) 280–287.

[5]   H.K. Boparai, M. Joseph, D.M. O'Carroll, Cadmium (Cd^{2+}) removal by nano zerovalent iron: surface analysis, effects of solution chemistry and surface complexation modeling, Environ. Sci. Pollut. Res. Int. 20 (2013) 6210–6221.

[6]   X. Gong, D. Huang, Y. Liu, G. Zeng, R. Wang, J. Wan, C. Zhang, M. Cheng, X. Qin, W. Xue, Stabilized nanoscale zerovalent iron mediated cadmium accumulation and oxidative damage of *Boehmeria nivea* (L.) Gaudich cultivated in cadmium contaminated sediments, Environ. Sci. Technol. 51 (2017) 11308–11316.

[7]   E. Smith, R. Naidu, A.M. Alston, Arsenic in the soil environment: a review, Adv. Agron. 64 (1998) 149-195.

[8]   S.R. Kanel, B. Manning, L. Charlet, H. Choi, Removal of arsenic (III) from groundwater by nanoscale zero-valent iron, Environ. Sci. Technol. 39 (2005) 1291–1298.

[9]   S.E. Baltazar, A. García, A.H. Romero, M. a. Rubio, N. Arancibia-Miranda, D. Altbir, Surface rearrangement of nanoscale zerovalent iron: the role of pH and its implications in the kinetics of arsenate sorption, Environ. Technol. 35 (2014) 2365–2372.

[10]   J. Silva-Yumi, M. Escudey, M. Gacitua, C. Pizarro, Kinetics, adsorption and desorption of Cd(II) and Cu(II) on natural allophane: effect of iron oxide coating, Geoderma. 319 (2018) 70–79.

[11]   Q. Yu, J.B. Fein, Enhanced removal of dissolved Hg(II), Cd(II), and Au(III) from water by *Bacillus subtilis* bacterial biomass containing an elevated concentration of sulfhydryl sites, Environ. Sci. Technol. 51 (2017) 14360–14367.

[12]   C. Cao, Q. Zhang, Z.-B. Ma, X.-M. Wang, H. Chen, J.-J. Wang, Fractionation and

526   mobility risks of heavy metals and metalloids in wastewater-irrigated agricultural soils

527   from greenhouses and fields in Gansu, China, Geoderma. 328 (2018) 1-9.

528   [13]   F. Fu, D.D. Dionysiou, H. Liu, The use of zero-valent iron for groundwater

529   remediation and wastewater treatment: a review, J. Hazard. Mater. 267 (2014) 194–

530   205.

531   [14]   M. Molina-Roco, M. Escudey, M. Antilén, N. Arancibia-Miranda, K. Manquián-

532   Cerda, Distribution of contaminant trace metals inadvertently provided by phosphorus

533   fertilisers: movement, chemical fractions and mass balances in contrasting acidic soils,

534   Environ. Geochem. Health. 40 (2018) 2491–2509.

535   [15]   M. Molina, K. Manquian-Cerda, M. Escudey, Sorption and selectivity sequences of

536   Cd, Cu, Ni, Pb, and Zn in single- and multi-component systems in a cultivated Chilean

537   Mollisol, Soil Sediment Contam. 19 (2010) 405–418.

538   [16]   M. Escudey, J.E. Förster, J.P. Becerra, M. Quinteros, J. Torres, N. Arancibia, G.

539   Galindo, A.C. Chang, Disposal of domestic sludge and sludge ash on volcanic soils, J.

540   Hazard. Mater. 139 (2007) 550–555.

541   [17]   P. Sipos, T. Németh, V.K. Kis, I. Mohai, Sorption of copper, zinc and lead on soil

542   mineral phases, Chemosphere. 73 (2008) 461–469.

543   [18]   N. Arancibia-Miranda, J. Silva-Yumi, M. Escudey, Effect of cations in the background

544   electrolyte on the adsorption kinetics of copper and cadmium and the isoelectric point

545   of imogolite, J. Hazard. Mater. 299 (2015) 675-684.

546   [19]   S.J. Bradfield, P. Kumar, J.C. White, S.D. Ebbs, Zinc, copper, or cerium accumulation

547   from metal oxide nanoparticles or ions in sweet potato: yield effects and projected

548   dietary intake from consumption, Plant Physiol. Biochem. 110 (2017) 128-137.

549   [20]   P.A. Kobielska, A.J. Howarth, O.K. Farha, S. Nayak, Metal–organic frameworks for

550   heavy metal removal from water, Coord. Chem. Rev. 358 (2018) 92–107.

551 [21] A.A. El-Kady, M.A. Abdel-Wahhab, Occurrence of trace metals in foodstuffs and their

552 health impact, Trends Food Sci. Technol. 75 (2018) 36–45.

553 [22] WHO, Guidelines for drinking-water quality, 4th edition, WHO Library Cataloguing-

554 in-Publication Data, World Health Organization (2011).

555 [23] W. Yan, M.A. V Ramos, B.E. Koel, W.X. Zhang, As(III) sequestration by iron

556 nanoparticles: study of solid-phase redox transformations with X-ray photoelectron

557 spectroscopy, J. Phys. Chem. C. 116 (2012) 5303–5311.

558 [24] N. Arancibia-Miranda, S.E. Baltazar, A. Garccía, D. Muñoz-Lira, P. Sepúlveda, M.A.

559 Rubio, D. Altbir, Nanoscale zero valent supported by zeolite and montmorillonite:

560 template effect of the removal of lead ion from an aqueous solution, J. Hazard. Mater.

561 301 (2016) 371–380.

562 [25] M. Stefaniuk, P. Oleszczuk, Y.S. Ok, Review on nano zerovalent iron (nZVI): from

563 synthesis to environmental applications, Chem. Eng. J. 287 (2016) 618-632.

564 [26] P. Sepúlveda, M.A. Rubio, Samuel E. Baltazar, J. Rojas-Nunez, J.L. Sánchez

565 Llamazares, Alejandra García Garcia, Nicolás Arancibia-Miranda, As(V) removal

566 capacity of FeCu bimetallic nanoparticles in aqueous solutions: the influence of Cu

567 content and morphologic changes in bimetallic nanoparticles, J. Colloid Interface Sci.

568 524 (2018) 177–187.

569 [27] N. Arancibia-Miranda, M. Escudey, R. Ramírez, R.I. González, A.C.T. van Duin, M.

570 Kiwi, Advancements in the synthesis of building block materials: experimental

571 evidence and modeled interpretations of the effect of Na and K on imogolite synthesis,

572 J. Phys. Chem. C. 121 (2017) 12658−12668.

573 [28] N. Arancibia-Miranda, M. Escudey, C. Pizarro, J.C. Denardin, M.T. García-González,

574 J.D. Fabris, L. Charlet, Preparation and characterization of a single-walled

575 aluminosilicate nanotube-iron oxide composite: its applications to removal of aqueous

576   arsenate, Mater. Res. Bull. 51 (2014) 145-152.

577   [29]   M. Boyer, E. Paineau, M. Bacia-Verloop, A. Thill, Aqueous dispersion state of

578   amphiphilic hybrid aluminosilicate nanotubes, Appl. Clay Sci. 96 (2014) 45–49.

579   [30]   A. Thill, P. Maillet, B. Guiose, O. Spalla, L. Belloni, P. Chaurand, M. Auffan, L.

580   Olivi, J. Rose, Physico-chemical control over the single- or double-wall structure of

581   aluminogermanate imogolite-like nanotubes, J. Am. Chem. Soc. 134 (2012) 3780–

582   3786.

583   [31]   E. Bahadori, V. Vaiano, S. Esposito, M. Armandi, D. Sannino, B. Bonelli, Photo-

584   activated degradation of tartrazine by H_2O_2 as catalyzed by both bare and Fe-doped

585   methyl-imogolite nanotubes, Catalysis Today. 304 (2017) 199-207.

586   [32]   Y.-H. Pan, Q.-Y. Zhao, L. Gu, Q.-Y. Wu, Thin film nanocomposite membranes based

587   on imologite nanotubes blended substrates for forward osmosis desalination,

588   Desalination. 421 (2017) 160–168.

589   [33]   P.D.G. Cradwick, V.C. Farmer, J.D. Russell, C.R. Masson, K. Wada, N. Yoshinaga,

590   Imogolite, a hydrated aluminium silicate of tubular structure, Nature, Phys. Sci. 240

591   (1972), 187.

592   [34]   G.I. Yucelen, R.P. Choudhury, J. Leisen, S. Nair, H.W. Beckham, Defect structures in

593   aluminosilicate single-walled nanotubes: a solid-state nuclear magnetic resonance

594   investigation, J. Phys. Chem. C. 116 (2012) 17149–17157.

595   [35]   N. Arancibia-Miranda, M. Escudey, M. Molina, M.T. García-González, Use of

596   isoelectric point and pH to evaluate the synthesis of a nanotubular aluminosilicate, J.

597   Non-Cryst. Solids. 357 (2011) 1750-1756.

598   [36]   J. P. Gustafsson, The surface chemistry of imogolite, Clays Clay Miner. 49 (2001) 73–

599   80.

600   [37]   C. Levard, E. Doelsch, J. Rose, A. Masion, I. Basile-Doelsch, O. Proux, J.-L.L.

26

601   Hazemann, D. Borschneck, J.-Y.Y. Bottero, Role of natural nanoparticles on the

602   speciation of Ni in andosols of la Reunion, Geochim. Cosmochim. Acta. 73 (2009)

603   4750–4760.

604   [38]   R. Rusmin, B. Sarkar, T. Tsuzuki, N. Kawashima, R. Naidu, Removal of lead from

605   aqueous solution using superparamagnetic palygorskite nanocomposite: material

606   characterization and regeneration studies, Chemosphere. 186 (2017) 1006–1015.

607   [39]   V.C. Farmer, A.R. Fraser, J.M. Tait, Synthesis of imogolite: a tubular aluminium

608   silicate polymer, J. Chem. Soc. Chem. Commun. 0 (1977) 462–463.

609   [40]   L. Denaix, I. Lamy, J. Yves, Synthetic colloidal amorphous aluminosilicates and their

610   precursors, Colloids Surf. A. 158 (1999) 315–325.

611   [41]   J. Hunter, Zeta Potential in Colloid Science: Principles and Applications, Academic

612   Press, London, 1981.

613   [42]   S. Azizian, Kinetic models of sorption: a theoretical analysis, J. Colloid Interface Sci.

614   276 (2004) 47–52.

615   [43]   S. Y. Lagergren, Zur theorie der sogenannten adsorption gelöster stoffe, Kungliga

616   Svenska Vetenskapsakad, Handlingar. 24 (1898) 1–39.

617   [44]   Y.S. Ho, Selection of optimum sorption isotherm, Carbon 42 (2004) 2115–2116.

618   [45]   Y.S. Ho, G. McKay, Pseudo-second order model for sorption processes, Process

619   Biochem. 34 (1999) 451–465.

620   [46]   W.J. Weber, J.C. Morris, Kinetics of adsorption on carbon from solution, ACSE J.

621   Sanit. Eng. Div. 89 (1963) 31–60.

622   [47]   L. Cáceres-Jensen, J. Rodríguez-Becerra, J. Parra-Rivero, M. Escudey, L. Barrientos,

623   V. Castro-Castillo, Sorption kinetics of diuron on volcanic ash derived soils, J. Hazard.

624   Mater. 261 (2013) 602–613.

625   [48]   G.I. Yucelen, D.-Y. Kang, I. Schmidt-Krey, H.W. Beckham, S. Nair, A generalized

626   kinetic model for the formation and growth of single-walled metal oxide nanotubes,

627   Chem. Eng. Sci. 90 (2013) 200–212.

628   [49]   A. Thill, B. Guiose, M. Bacia-Verloop, V. Geertsen, L. Belloni, How the diameter and

629   structure of $(OH)_3Al_2O_3Si_xGe_{1-x}OH$ imogolite nanotubes are controlled by an adhesion

630   versus curvature competition, J. Phys. Chem. C. 116 (2012) 26841–26849.

631   [50]   C. Pizarro, M.A. Rubio, M. Escudey, M.F. Albornoz, D. Muñoz, J. Denardin, J.D.

632   Fabris, C. Pizarro, M.A. Rubio, M. Escudey, M.F. Albornoz, D. Muñoz, J. Denardin,

633   J.D. Fabris, Nanomagnetite-zeolite composites in the removal of arsenate from

634   aqueous systems, J. Braz. Chem. Soc. 26 (2015) 1887–1896.

635   [51]   F.J. Gil-Llambías, A.M. Escudey-Castro, Use of zero point charge measurements in

636   determining the apparent surface coverage of molybdena in MoO_3/γ-Al_2O_3 catalysts, J.

637   Chem. Soc., Chem. Commun. 0 (1982) 478–479.

638   [52]   N. Arancibia-Miranda, M. Escudey, M. Molina, M.T. García-González, Kinetic and

639   surface study of single-walled aluminosilicate nanotubes and their precursors,

640   Nanomaterials. 3 (2013) 126–140.

641   [53]   E. Shafia, S. Esposito, M. Armandi, M. Manzoli, E. Garrone, B. Bonelli, Isomorphic

642   substitution of aluminium by iron into single-walled alumino-silicate nanotubes: a

643   physico-chemical insight into the structural and adsorption properties of Fe-doped

644   imogolite, Microporous Mesoporous Mater. 224 (2016) 229–238.

645   [54]   W.C. Ackerman, D.M. Smith, J.C. Huling, Y. Kim, J.K. Bailey, C.J. Brinker,

646   Gas/vapor adsorption in imogolite: a microporous tubular aluminosilicate, Langmuir. 9

647   (1993) 1051–1057.

648   [55]   N. Arancibia-Miranda, S.E. Baltazar, A. García, A.H. Romero, M. a. Rubio, D. Altbir,

649   Lead removal by nano-scale zero valent iron: surface analysis and pH effect, Mater.

650   Res. Bull. 59 (2014) 341–348.

651   [56]   R. Rusmin, B. Sarkar, Y. Liu, S. McClure, R. Naidu, Structural evolution of chitosan–

652   palygorskite composites and removal of aqueous lead by composite beads, Appl. Surf.

653   Sci. 353 (2015) 363–375.

654   [57]   K. Manquián-Cerda, E. Cruces, M. Angélica Rubio, C. Reyes, N. Arancibia-Miranda,

655   Preparation of nanoscale iron (oxide, oxyhydroxides and zero-valent) particles derived

656   from blueberries: reactivity, characterization and removal mechanism of arsenate,

657   Ecotoxicol. Environ. Saf. 145 (2017) 69-77.

658   [58]   J.C. Raposo, M.A. Olazábal, J.M. Madariaga, Complexation and precipitation of

659   arsenate and iron species in sodium perchlorate solutions at 25 ºC, J. Solution Chem.

660   35 (2006) 79–94.

661   [59]   B. Nowack, T.D. Bucheli, Occurrence, behavior and effects of nanoparticles in the

662   environment, Environ. Pollut. 150 (2007) 5–22.

663   [60]   G. Limousin, J.-P. Gaudet, L. Charlet, S. Szenknect, V. Barthès, M. Krimissa, Sorption

664   isotherms: a review on physical bases, modeling and measurement, Appl. Geochem.

665   22 (2007) 249–275.

666   [61]   C.J. Clark, Cation and anion retention by natural and synthetic allophane and

667   imogolite, Clays Clay Miner. 32 (1984) 291–299.

668   [62]   C.J. Clark, M.B. Mcbride, Chemisorption of Cu(II) and Co(II) on allophane and

669   imogolite, Clays Clay Miner. 32 (1984) 300–310.

670   [63]   A. Morales, M. Cruells, A. Roca, R. Bergó, Treatment of copper flash smelter flue

671   dusts for copper and zinc extraction and arsenic stabilization, Hydrometallurgy. 105

672   (2010) 148–154.

673   [64]   S. Li, W. Wang, Y. Liu, W. xian Zhang, Zero-valent iron nanoparticles (nZVI) for the

674   treatment of smelting wastewater: a pilot-scale demonstration, Chem. Eng. J. 254

675   (2014) 115–123.

676 [65] J. Liu, P. Wu, S. Li, M. Chen, W. Cai, D. Zou, N. Zhu, Z. Dang, Synergistic deep

677 removal of As(III) and Cd(II) by a calcined multifunctional MgZnFe-CO$_3$ layered

678 double hydroxide: photooxidation, precipitation and adsorption, Chemosphere. 225

679 (2019) 115–125.

680 [66] R.A. Anayurt, A. Sari, M. Tuzen, Equilibrium, thermodynamic and kinetic studies on

681 biosorption of Pb(II) and Cd(II) from aqueous solution by macrofungus (*Lactarius*

682 *scrobiculatus*) biomass, Chem. Eng. J. 151 (2009) 255–261.

683 [67] M.J. Cooper, Synthetic imogolite: a product in search of a market, Technovation. 102

684 (1990) 69–71.

685 [68] B. Pan, H. Qiu, B. Pan, G. Nie, L. Xiao, L. Lv, W. Zhang, Q. Zhang, S. Zheng, Highly

686 efficient removal of heavy metals by polymer-supported nanosized hydrated Fe(III)

687 oxides: behavior and XPS study, Water Res. 44 (2010) 815–824.

688 [69] M. Vítkov, M. Puschenreiter, M. Kom Arek, Effect of nano zero-valent iron

689 application on As, Cd, Pb, and Zn availability in the rhizosphere of metal(loid)

690 contaminated soils, Chemosphere. 200 (2018) 217-226.

691 [70] H.K. Boparai, M. Joseph, D.M. O'Carroll, Kinetics and thermodynamics of cadmium

692 ion removal by adsorption onto nano zerovalent iron particles, J. Hazard. Mater. 186

693 (2011) 458–465.

694 [71] R.D. Shannon, Revised effective ionic radii and systematic studies of interatomic

695 distances in halides and chalcogenides. Acta Crystallogr., Sect. A: Found. Crystallogr.
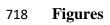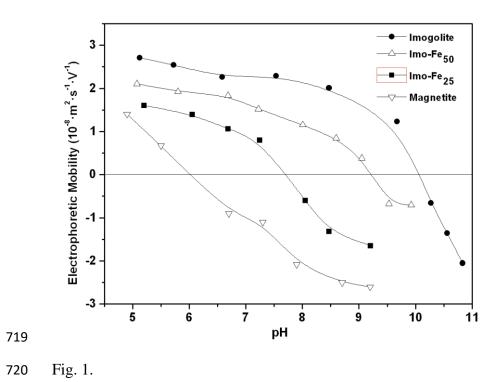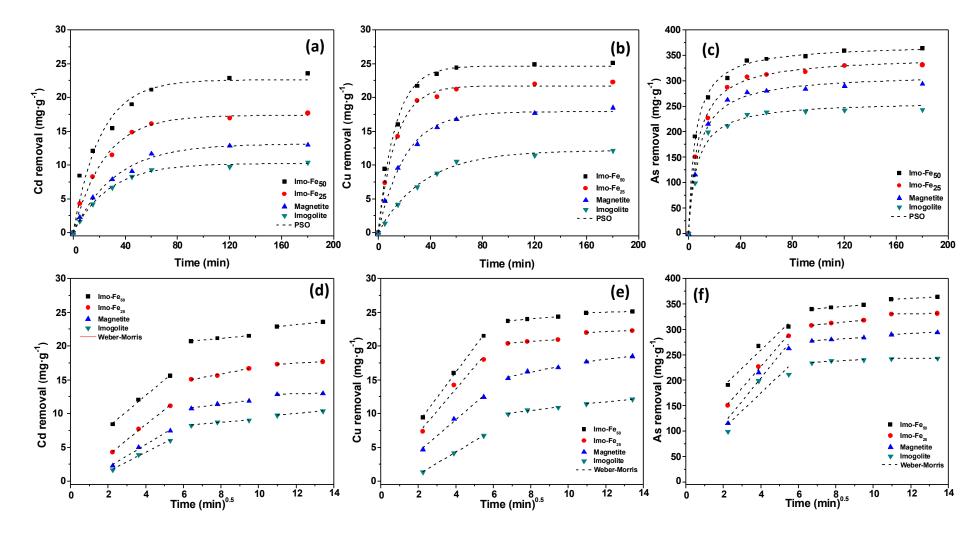
696 32 (1976) 751–67.

697

Figure captions

Fig. 1. Electrophoretic mobility vs. pH plots of imogolite, magnetite, Imo-Fe$_{25}$ and Imo-Fe$_{50}$.

Fig. 2. Kinetic adsorption of single components for (a) Cd, (b) Cu, and (c) As in all

substrates. Intraparticle diffusion plots for (d) Cd, (e) Cu, and (f) As adsorption on the

samples. Note that the axes have different scales.

Fig. 3. Adsorption isotherms in single and multi-components for (a) Cd, (b) Cd/Cu, (c)

Cd/Cu/As, (d) Cu, (e) Cu/Cd, and (f) Cu/Cd/As. The lines show Langmuir-Freundlich's fit.

Fig. 4. Adsorption isotherms in single and multi-components for (a) As and (b) As/Cu/Cd.

The lines show Langmuir-Freundlich's fit.

Fig. 5. Schematic diagram of the Cu, Cd and As removal mechanisms by imogolite and Imo-

Fe materials.

Table titles

Table 1. Kinetic parameters predicted from the pseudo-first order, pseudo-second order, and

intraparticle diffusion models.

Table 2. Related parameters for the adsorption of Cu and Cd on imogolite, magnetite, Imo-

Fe$_{25}$ and Imo-Fe$_{50}$.

Table 3. Related parameters for the adsorption of arsenic on imogolite, magnetite, Imo-Fe$_{25}$
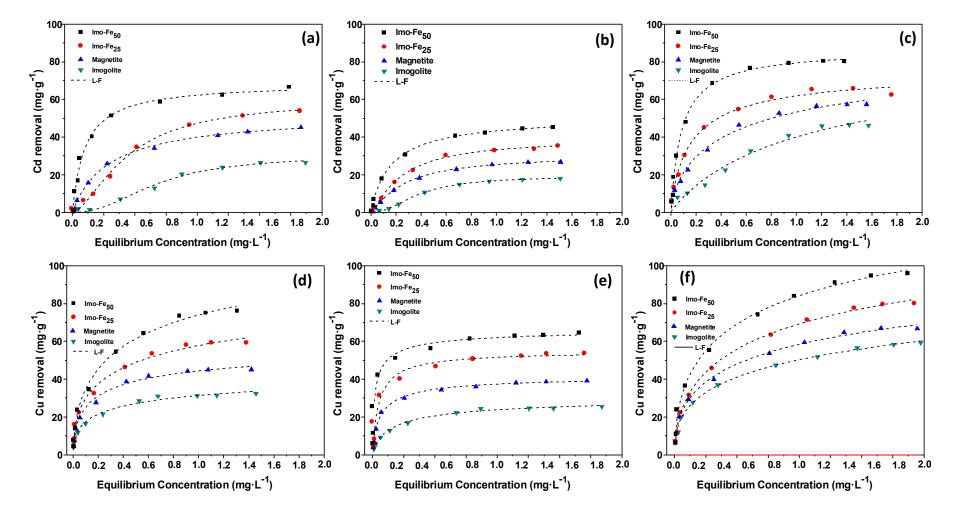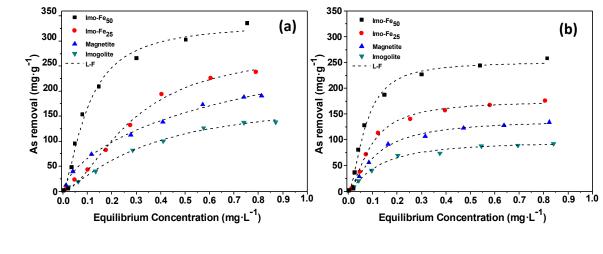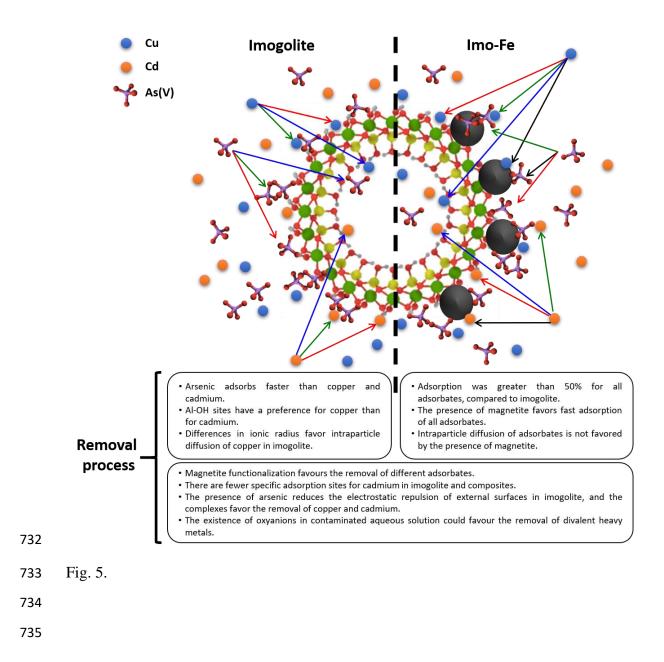
and Imo-Fe$_{50}$.

718   **Figures**

719

720   Fig. 1.

721

722

723   Fig. 2.

724

725

Fig. 3.

727

728

729

730   Fig. 4.

731

Fig. 5.

Tables

Table 1. Kinetic parameters predicted from the pseudo-first order, pseudo-second order, and intraparticle diffusion models.

Models	Cu	Cd	As	Cu	Cd	As	Cu	Cd	As	Cu	Cd	As
	Imogolite			Magnetite			Imo-Fe$_{25}$			Imo-Fe$_{50}$		
q_{exp} $(mg{\cdot}g^{-1})$	12.1	10.4	243.3	18.5	13.0	294.5	22.3	17.7	331.3	25.1	23.6	363.9
Pseudo-first order												
$C_{m\text{-}cal}$ $(mg{\cdot}g^{-1})$	14.9 (0.7)[*]	11.9 (0.6)	260.2 (5.6)	20.5 (2.0)	15.7 (1.0)	314.0 (20.5)	24.3 (0.7)	20.1 (0.8)	348.3 (4.3)	27.3 (0.85)	25.4 (0.7)	371.9 (4.8)
k_1 $(x10^{-3} min^{-1})$	2.8 (0.4)	3.7 (0.6)	109.4 (11.5)	4.8 (0.4)	3.1 (0.5)	95.8 (10.3)	7.1 (0.4)	3.8 (0.4)	97.2 (11.0)	7.5 (0.5)	4.8 (0.4)	112.8 (5.2)
r^2	0.983	0.984	0.967	0.995	0.980	0.981	0.985	0.985	0.979	0.985	0.984	0.981
RMSE	0.21	1.3	4.53	0.25	1.65	4.03	0.33	0.81	3.99	0.37	1.2	4.92
Pseudo-second order												
$C_{m\text{-}cal}$ $(mg{\cdot}g^{-1})$	12.7 (0.2)	9.1 (0.2)	237.2 (7.2)	17.9 (0.4)	13,1 (0.7)	285.4 (7.4)	21.7 (0.2)	17.4 (0.9)	317.7 (8.2)	24.7 (0.3)	22.7 (0.7)	342.3 (3.2)
k_2 $(x10^{-4} g{\cdot}mg^{-1}{\cdot}min^{-1})$	3.4 (0.1)	2.0 (0.1)	5.9 (0.9)	3.1 (0.5)	2.2 (0.6)	10.1 (0.5)	4.2 (0.7)	2.6 (0.5)	4.1 (0.3)	4.6 (0.8)	2.7 (0.3)	5.1 (0.4)
$h(mg{\cdot}g^{-1}{\cdot}min^{-1})$	0.07	0.05	39.99	0.13	0.05	131.30	0.25	0.11	48.53	0.34	0.17	70.53
r^2	0.993	0.991	0.994	0.993	0.988	0.994	0.990	0.991	0.997	0.991	0.992	0.996
RMSE	0.19	0.88	3.44	0.14	0.11	0.22	0.12	0.21	3.22	0.34	0.33	4.63
Intraparticle diffusion[#]												
$q_{e\text{-}2}$ $(mg{\cdot}g^{-1})$	4.1 (0.3)	3.0 (0.5)	29.6 (1.9)	4.4 (1.1)	5.9 (0.9)	21.4 (2.2)	2.9 (0.1)	5.6 (0.6)	32.1 (2.7)	2.8 (0.3)	5.9 (0.4)	45.0 (2.4)

k_{int-2} ($mg \cdot g^{-1} \cdot min^{1/2}$)	0.4 (0.1)	0.2 (0.1)	2.1 (0.3)	0.6 (0.1)	0.4 (0.1)	2.4 (0.6)	0.2 (0.0)	0.5 (0.1)	3.7 (0.2)	0.3 (0.0)	0.3 (0.0)	3.1 (0.1)
C_2 ($mg \cdot g^{-1}$)	7.7 (0.7)	6.8 (0.4)	220.7 (9.3)	11.6 (1.3)	8.5 (0.5)	261.5 (0.8)	19.1 (2.1)	11.6 (0.6)	283.3 (1.6)	22.2 (1.92)	19.1 (2.0)	319.3 (1.1)
r^2	0.992	0.994	0.995	0.985	0.969	0.993	0.989	0.975	0.996	0.989	0.982	0.993

738

739 [*] Values in parentheses correspond to standard errors.

740 [#] RMSE for intraparticle diffusion model was not calculated because the model does not give a relevant q_{e-cal} value. An approximation could be
741 made from the overall curve fitting, but that would be hardly feasible because the curve represents different diffusion processes.

742 **Table 2.** Related parameters for the adsorption of Cu and Cd on imogolite, magnetite, Imo-Fe$_{25}$ and Imo-Fe$_{50}$.

	Single-component Langmuir-Freundlich					Multi-component (Cu+Cd) Langmuir-Freundlich					Multi-component (Cu+Cd+As) Langmuir-Freundlich				
	Q_{sat}	K	n	r^2	RMSE	Q_{sat}	K	n	r^2	RMSE	Q_{sat}	K	n	r^2	RMSE
Copper (Cu)															
Imogolite	52.0 (4.1)[*]	1.5 (0.34)	0.5 (0.0)	0.985	0.092	31.8 (2.5)	3.8 (1.0)	0.7 (0.1)	0.991	0.231	132.6 (9.1)	0.6 (0.0)	0.4 (0.1)	0.970	0.069
Magnetite	61.2 (5.9)	2.6 (0.7)	0.6 (0.2)	0.989	0.108	42.4 (1.9)	8.9 (2.4)	0.8 (0.1)	0.902	0.115	151.9 (19.9)	0.9 (0.1)	0.5 (0.0)	0.993	0.074
Imo-Fe$_{25}$	105.6 10.3)	1.5 (0.3)	0.7 (0.1)	0.989	0.142	54.9 (3.2)	13.7 (1.9)	0.9 (0.1)	0.989	0.099	157.9 (20.9)	0.9 (0.1)	0.5 (0.1)	0.973	0.103
Imo-Fe$_{50}$	131.7 (12.9)	1.5 (0.5)	0.7 (0.1)	0.990	0.170	67.1 (5.9)	18.0 (0.8)	0.9 (0.1)	0.992	0.187	169.3 (22.9)	1.1 (0.1)	0.5 (0.1)	0.976	0.123
Cadmium (Cd)															
Imogolite	30.5 (3.1)	3.9 (1.0)	2.2 (0.4)	0.993	0.145	19.2 (1.0)	7.8 (1.1)	2.1 (0.3)	0.993	0.075	76.6 (6.7)	4.2 (0.3)	0.8 (0.1)	0.955	0.092
Magnetite	52.8 (2.9)	3.8 (0.5)	1.0 (0.2)	0.992	0.099	30.5 (1.2)	5.0 (0.6)	1.2 (0.1)	0.998	0.122	86.4 (9.7)	0.8 (0.1)	0.9 (0.1)	0.986	0.088
Imo-Fe$_{25}$	60.2 (3.4)	5.3 (0.8)	1.2 (0.2)	0.996	0.078	39.3 (1.9)	5.4 (0.7)	1.5 (0.2)	0.993	0.101	87.1 (3.6)	7.4 (0.9)	1.0 (0.0)	0.955	0.143
Imo-Fe$_{50}$	68.8 (2.9)	11.1 (1.0)	1.5 (0.3)	0.990	0.085	51.9 (2.4)	6.2 (0.6)	1.7 (0.6)	0.994	0.152	92.5 (3.9)	8.6 (1.9)	1.2 (0.0)	0.956	0.084

743

744 [*] Values in parentheses correspond to standard errors.

745   **Table 3.** Related parameters for the adsorption of arsenic on imogolite, magnetite, Imo-Fe$_{25}$ and Imo-Fe$_{50}$.

| | Single-component | | | | | Multi-component | | | | |
| | Langmuir-Freundlich | | | | | Langmuir-Freundlich | | | | |
	Q_{sat}	K	n	r^2	RMSE	Q_{sat}	K	n	r^2	RMSE
Imogolite	186.7 (33.3)[*]	3.8 (0.7)	1.3 (0.4)	0.989	0.112	98.7 (11.7)	15.5 (1.8)	1.3 (0.39)	0.990	0.099
Magnetite	285.9 (27.2)	8.4 (1.7)	1.7 (0.3)	0.990	0.078	139.4 (9.7)	15.6 (1.8)	1.4 (0.39)	0.991	0.099
Imo-Fe$_{25}$	335.9 (11.2)	31.3 (9.8)	1.7 (0.3)	0.991	0.075	175.5 (8.36)	48.7 (7.66)	1.6 (0.27)	0.989	0.101
Imo-Fe$_{50}$	472.9 (32.9)	32.9 (3.50)	1.8 (0.2)	0.989	0.111	251.6 (6.7)	103.9 (23.9)	1.7 (0.2)	0.991	0.101

746

747   [*] Values in parentheses correspond to standard errors.

748

749   **Supporting Information:**

750   **Mechanistic insights into simultaneous removal of copper, cadmium and arsenic from**

751   **water by iron oxide-functionalized magnetic imogolite nanocomposites**

752

753   Nicolás Arancibia-Miranda[a,b*], Karen Manquián-Cerda[b], Carmen Pizarro[b], Tamara Maldonado[b],

754   Jonathan Suazo-Hernández[c], Mauricio Escudey[a,b], Nanthi Bolan[d], Binoy Sarkar[e*]

755

756   [a] Center for the Development of Nanoscience and Nanotechnology, CEDENNA, 9170124,

757   Santiago, Chile

758   [b] Facultad de Química y Biología, Universidad de Santiago de Chile, Av. B. O'Higgins, 3363,

759   Santiago, Chile

760   [c] Programa de Doctorado en Ciencias de Recursos Naturales Universidad de La Frontera,

761   (BIOREN-UFRO), Universidad de La Frontera, Avenida Francisco Salazar 01145, Temuco,

762   Chile

763   [d] Global Centre for Environmental Remediation (GCER), Advanced Technology Centre, Faculty

764   of Science, The University of Newcastle, Callaghan, NSW 2308, Australia

765   [e] Lancaster Environment Centre, Lancaster University, Lancaster, LA1 4YQ, UK

766

767   [*] Co-corresponding authors:

768   Dr Binoy Sarkar; Lancaster University; e-mail: b.sarkar@lancaster.ac.uk, and

769   Dr Nicolás Arancibia-Miranda; Universidad de Santiago de Chile; e-mail:
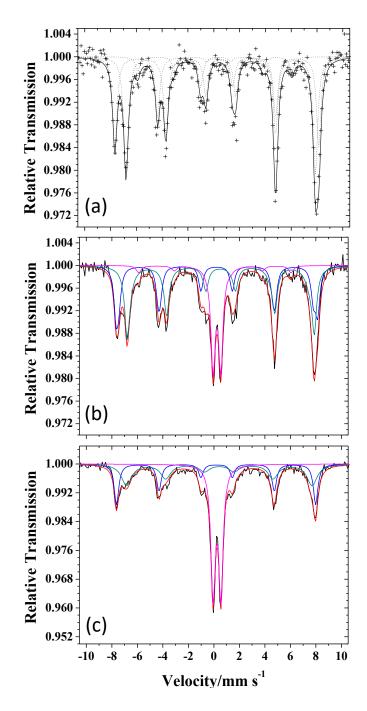
770   nicolas.arancibia@usach.cl

771

772

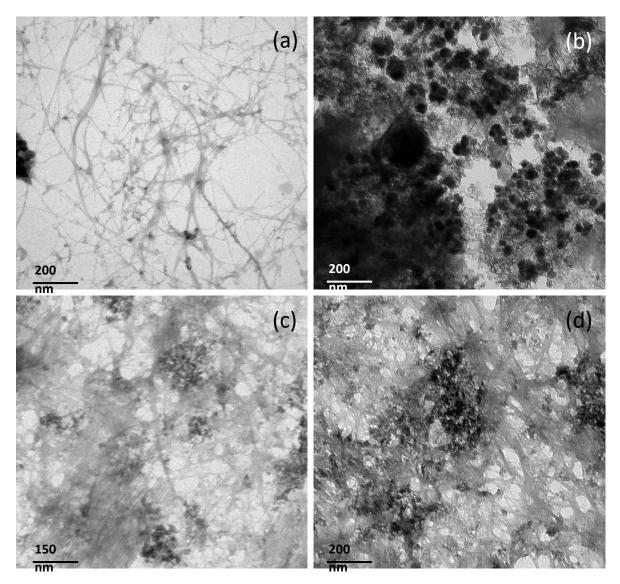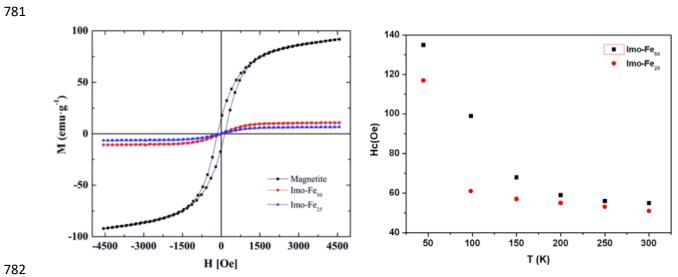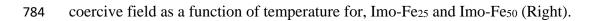**Fig. S1.** 298 K-Mössbauer spectra at ambient temperature: (a) magnetite, (b) Imo-Fe$_{25}$, (c) Imo-Fe$_{50}$.

Fig. S2. TEM images of: (a) Imogolite, (b) magnetite, (c) Imo-Fe$_{25}$, and (d) Imo-Fe$_{50}$.

781

782
783 **Fig. S3.** Magnetization response of Imogolite, Imo-Fe$_{25}$ and Imo-Fe$_{50}$ (Left). Evolution of the

784 coercive field as a function of temperature for, Imo-Fe$_{25}$ and Imo-Fe$_{50}$ (Right).

785
786

787   **Table S1.** 298 K Mössbauer fitted parameters for the a) nano-magnetite, (b) Imo-Fe$_{25}$, (c) Imo-Fe$_{50}$.

Sample	Assignment	δ/mm s^{-1}	ε, Δ/mm s^{-1}	Γ/mm s^{-1}	B_{hf}/T	RA/%
	[MG]	0.332(7)	0.01(1)	0.41(2)	49.01(5)	40(2)
Nano-magnetite	{MG}	0.640(5)	-0.001(1)	0.41(2)	45.49(4)	51(2)
	α-FeOOH	0.32(4)	-0.27(8)	0.40(1)	37.0(3)	9(2)
	[MG]	0.318(4)	-0.042(9)	0.42(2)	48.72(4)	33(3)
	{MG}	0.590(3)	0.00*	0.68(6)	45.22(4)	40(2)
Imo-Fe$_{25}$	(Super) paramagnetic Fe(III)	0.351(4)	0.71(5)	0.44(2)	--	18(5)
	(Super) paramagnetic Fe(III)	0.349(3)	0.50(1)	0.22(2)	--	9(5)
	[MG]	0.304(5)	-0.042(9)	0.42(2)	48.43(4)	28(1)
	{MG}	0.54(1)	0.00*	0.96(6)	45.02(1)	31(2)
Imo-Fe$_{50}$	(Super) paramagnetic Fe(III)	0.355(4)	0.73(5)	0.49(2)	--	30(5)
	(Super) paramagnetic Fe(III)	0.356(3)	0.50(1)	0.23(4)	--	11(5)

788

789   **Table S2.** Specific surface area and porosity parameters of imogolite and Imogolite, Imo-Fe$_{25}$
790   and Imo-Fe$_{50}$.

	Imogolite	**Magnetite**	**Imo-Fe$_{25}$**	**Imo-Fe$_{50}$**
Specific surface area (m²·g^{-1})	310	87	265	203
External surface area (m²·g^{-1})	180	35	149	117
Micropore volume x10^{-3} (cm³·g^{-1})	20	1.5	22	30
Micropore area (m²·g^{-1})	66	17	53	46
Pore Volume (cm³·g^{-1})	0.25	0.18	0.24	0.20
Pore diameter (Å)	10	18	11	15

791
792

793 **Table S3.** Experimental maximums of Cu and Cd adsorption in different systems studied.

Sample	Single-component	Multi-component (Cu+Cd)	% Difference*	Multi-component (Cu+Cd+As)
Copper - Experimental Maximum Adsorption (mg/g)				
Imogolite	50.2	31.8	36.7	132.6
Magnetite	61.2	42.4	30,7	151.9
Imo-Fe$_{25}$	105.6	54.9	48.0	157.9
Imo-Fe$_{50}$	131.7	67.1	49.1	16.3
Cadmium - Experimental Maximum Adsorption (mg/g)				
Imogolite	30,5	19,2	37,0	76.6
Magnetite	52,8	30,5	42,2	86.4
Imo-Fe$_{25}$	60,2	39,3	34,7	87.1
Imo-Fe$_{50}$	68,8	51,9	24,6	92.5

794

795 * Percentage difference of amount adsorbed between single and multi-component systems with
796 respect to single-component adsorption

797